Journal of
Synchrotron Radiation
ISSN 1600-5775

The power of *in situ* pulsed laser deposition synchrotron characterization for the detection of domain formation during growth of $Ba_{0.5}Sr_{0.5}TiO_3$ on MgO

Sondes Bauer, Sergey Lazarev, Alan Molinari, Andreas Breitenstein, Philipp Leufke, Robert Kruk, Horst Hahn and Tilo Baumbach

J. Synchrotron Rad. (2014). **21**, 386–394

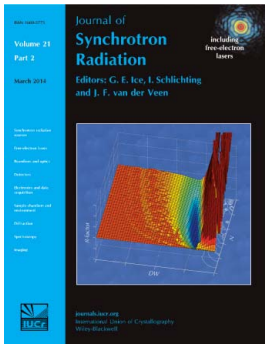

Journal of
Synchrotron Radiation

ISSN 1600-5775

Received 1 November 2013
Accepted 20 December 2013

The power of *in situ* pulsed laser deposition synchrotron characterization for the detection of domain formation during growth of $Ba_{0.5}Sr_{0.5}TiO_3$ on MgO

Sondes Bauer,[a]* Sergey Lazarev,[a] Alan Molinari,[b] Andreas Breitenstein,[a] Philipp Leufke,[b] Robert Kruk,[b] Horst Hahn[b] and Tilo Baumbach[a]

[a]Synchrotron Facility ANKA, Karlsruhe Institute of Technology, Hermann-von-Helmholtz-Platz 1, 76344 Eggenstein-Leopoldshafen, Germany, and [b]Institute for Nanotechnology, Karlsruhe Institute of Technology, Hermann-von-Helmholtz-Platz 1, 76344 Eggenstein-Leopoldshafen, Germany. *E-mail: sondes.bauer@kit.edu

A highly sophisticated pulsed laser deposition (PLD) chamber has recently been installed at the NANO beamline at the synchrotron facility ANKA (Karlsruhe, Germany), which allows for comprehensive studies on the PLD growth process of dielectric, ferroelectric and ferromagnetic thin films in epitaxial oxide heterostructures or even multilayer systems by combining *in situ* reflective high-energy diffraction with the *in situ* synchrotron high-resolution X-ray diffraction and surface diffraction methods. The modularity of the *in situ* PLD chamber offers the opportunity to explore the microstructure of the grown thin films as a function of the substrate temperature, gas pressure, laser fluence and target–substrate separation distance. $Ba_{0.5}Sr_{0.5}TiO_3$ grown on MgO represents the first system that is grown in this *in situ* PLD chamber and studied by *in situ* X-ray reflectivity, *in situ* two-dimensional reciprocal space mapping of symmetric X-ray diffraction and acquisition of time-resolved diffraction profiles during the ablation process. *In situ* PLD synchrotron investigation has revealed the occurrence of structural distortion as well as domain formation and misfit dislocation which all depend strongly on the film thickness. The microstructure transformation has been accurately detected with a time resolution of 1 s. The acquisition of two-dimensional reciprocal space maps during the PLD growth has the advantage of simultaneously monitoring the changes of the crystalline structure as well as the formation of defects. The stability of the morphology during the PLD growth is demonstrated to be remarkably affected by the film thickness. A critical thickness for the domain formation in $Ba_{0.5}Sr_{0.5}TiO_3$ grown on MgO could be determined from the acquisition of time-resolved diffraction profiles during the PLD growth. A splitting of the diffraction peak into two distinguishable peaks has revealed a morphology change due to modification of the internal strain during growth.

Keywords: *in situ* pulsed laser deposition; *in situ* synchrotron X-ray diffraction; *in situ* structural characterization; 2D-reciprocal space mapping; growth of $BaSrTiO_3$.

1. Introduction

There is a great interest in device applications based on $Ba_xSr_{(1-x)}TiO_3$ (BST, x) thin films. Chen *et al.* (2001) pointed out that pulsed laser deposition (PLD) growth of epitaxial ferroelectric (BST, x) thin films on $LaAlO_3$ and MgO substrates leads to the formation of material with dielectric properties useful for various high-performance microwave devices. The Curie temperature T_C, the dielectric properties, the fatigue behavior and the loss tangent of (BST, x) depend on the ratio between Ba and Sr (Jang *et al.*, 1997; Kim *et al.*, 1994). Their studies of (BST, x) with $x < 0.7$ have demonstrated a paraelectric behavior with a low level of fatigue at room temperature, which is required for the development of dynamic random-access memories. A large electric field effect at room temperature was measured in the case of solid solutions of dielectric (BST, x) thin films with a doping of $0.4 \leq x \leq 0.6$ in (BST, x) (Findikoglu *et al.*, 1997; Jia *et al.*, 1999). According to Okatan *et al.* (2008), it is difficult to simultaneously achieve high tunability (>40%) over a large

temperature range from 253 K to 358 K together with low dielectric losses over a huge operational bandwidth up to 30 GHz. It has been demonstrated that the dielectric constant and the loss tangent of (BST, x) films strongly depend on the film thickness and quality (Chen *et al.*, 2006). The latter is influenced by the choice of the substrate material, as it determines the presence of fine-sized grains (McNeal *et al.*, 1998), particularly at the interface (Lee & Hwang, 2000), as well as surface behavior in general, especially for large lattice misfit substrates such as MgO. The large lattice misfit of around −6% between (BST, x) and MgO requires a high density of edge dislocations at the interface to release the misfit energy. Thus, the strain energy makes it difficult to grow epitaxial (BST, x) films on MgO substrates. Moreover, a significant influence of the structural distortion of epitaxial (BST, x) thin films on the dielectric properties such as dielectric constant and tunability has been observed (Alldredge *et al.*, 2007).

High-resolution transmission electron microscopy (HRTEM) and selected-area electron diffraction (SAED), where the pattern is taken from the area covering the film and the substrate, have significantly contributed to understanding the strong influence exerted on the microstructure of the films by the surface structure of the substrates, such as surface-terrace, miscut angles, as well as step height and dimensions (Jiang *et al.*, 2002). Jiang *et al.* (2002) reported that the initial forming layer of a (BST, x) film on MgO (001) is in fact a TiO_2 monolayer, that acts as a nucleation layer. Lin & Chen (2009) have described the growth of the (BST, x) thin film on (001) MgO in such a way: ''the hetero-epitaxial BSTO film on each terrace becomes a single domain and the film consists of many domains which are shifted by a half unit cell along the *c*-axis direction if the neighboring terraces are single-step-height terraces. The antidomain boundaries are therefore formed at the boundary of each step terrace'' (Lin & Chen, 2009; Chen *et al.*, 2001).

In spite of much progress in investigating the domain formation in epitaxial (BST, x) thin films which are originating from the step height of the substrate surface terraces, the relation between the film thickness, which influences the dielectric properties, and the domain formation during the hetero-epitaxial growth has not yet been fully understood. As far as we know, no study has been reported on the evolution of the domains during the growth, nor on the critical film thickness necessary for the domains formation. Currently several research groups around the world are pursuing time-resolved surface-sensitive X-ray scattering studies of PLD growth. The first of these experiments was performed by a group from Oak Ridge at the Advanced Photon Source (Eres *et al.*, 2002; Tischler *et al.*, 2006), investigating $SrTiO_3$ (001) homoepitaxy. Another PLD chamber dedicated to the thin-film growth laboratory and beamline at the Cornell High Energy Synchrotron Source was used to study homoepitaxy and heteroepitaxy (Dale *et al.*, 2006; Fleet *et al.*, 2006). The thin-film growth/time-resolved X-ray diffraction facility in the G3 experimental station at the Cornell High Energy Synchrotron Source was used for *in situ* X-ray reflectivity measurements with the goal of real-time monitoring of film thickness and roughness during the growth (Wang *et al.*, 2004).

A group from the Paul Scherrer Institute has developed a PLD chamber at the Swiss Light Source for the growth of colossal magnetoresistance materials (Willmott *et al.*, 2005, 2006). The first time-resolved measurements of PLD growth were carried out at the European Synchrotron Radiation Facility (Vonk *et al.*, 2005) on the homoepitaxial growth of $SrTiO_3$. In summary, there is great interest in *in situ* time-resolved studies of structural changes during the PLD growth of materials with the aim to optimize their physical properties.

In the present work, *in situ* PLD was performed at the NANO beamline at the synchrotron facility ANKA (Karlsruhe, Germany) to determine the critical thickness that leads to the structural distortion as well as to domain formation of (BST, $x = 0.5$) grown on (001) MgO, as revealed by the combination of X-ray reflectivity (XRR) and the acquisition of two-dimensional reciprocal space maps (2D-RSMs) of a symmetric reflection during the PLD growth process.

2. Experiment

2.1. PLD growth of $Ba_{0.5}Sr_{0.5}TiO_3$

$Ba_{0.5}Sr_{0.5}TiO_3$ (BST, $x = 0.5$) thin films were grown on MgO (100) substrates by PLD, using a frequency-quadrupled (266 nm) Nd:YAG laser operated at a repetition rate of 10 Hz. A pulse duration of 5 ns and a single pulse energy of 90 mJ per pulse were used. The laser was focused to a spot of size 2 mm × 2 mm which led to a fluence of 2.4 J cm^{-2}. The average laser power was 1 W at 10 Hz.

After applying 600 laser pulses, the growth was interrupted in order to measure XRR and 2D-RSMs. The total pulse duration corresponded to 1 min of growth while the whole X-ray measurements were performed in about 10 min in total.

The (BST, $x = 0.5$) target, supplied by SurfaceNet (Rheine, Germany), with a purity of 99.9% was rotated at 8 r.p.m. during the ablation process. The substrate was positioned 4 cm from the target and heated to 1023 K using a laser heater with an integrated pyrometer for temperature sensing by an infrared diode laser with a spot size diameter of approximately 10 mm. A high-speed pyrometer with a sample rate of up to 10 kHz was used to control the substrate temperature, ensuring high-temperature stability. The pressure of the oxygen gas was set to 0.067 mbar (*i.e.* 6.7 Pa, 51 mTorr), precisely adjusted by the interplay of a fully open leak valve and a mass-flow controller. The growth of (BST, $x = 0.5$) on the MgO substrate took about 105 min.

2.2. Description of the *in situ* PLD–diffractometer system at the NANO beamline

We have recently developed a PLD chamber dedicated to *in situ* structural characterization during the growth process using *in situ* high-resolution X-ray diffraction and *in situ* surface scattering methods. The chamber was built by the company Surface (Hückelhoven, Germany) and delivered to

the synchrotron facility ANKA (Karlsruhe, Germany) in April 2013 to be installed on the NANO beamline. The essential feature of this sophisticated PLD chamber is the ability to perform correlated investigations involving *in situ* X-ray synchrotron and *in situ* RHEED studies with the goal of understanding the influence of growth parameters on the growth mode and on the final structure of (epitaxial) thin films. Figs. 1(*a*) and 1(*b*) show three-dimensional models of the PLD growth chamber from the beam entrance and exit, respectively. In contrast to standard PLD chambers used at laboratories, our *in situ* X-ray diffraction PLD chamber contains high-purity beryllium windows allowing for X-ray transmission. The entrance beryllium window has a horizontal angular opening of 55°, while the exit beryllium window, built in an L-shape, has vertical and horizontal openings of 55° and 70°, respectively.

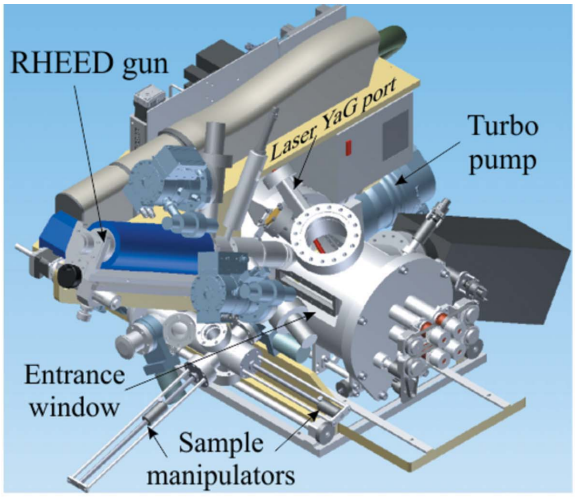

(*a*)

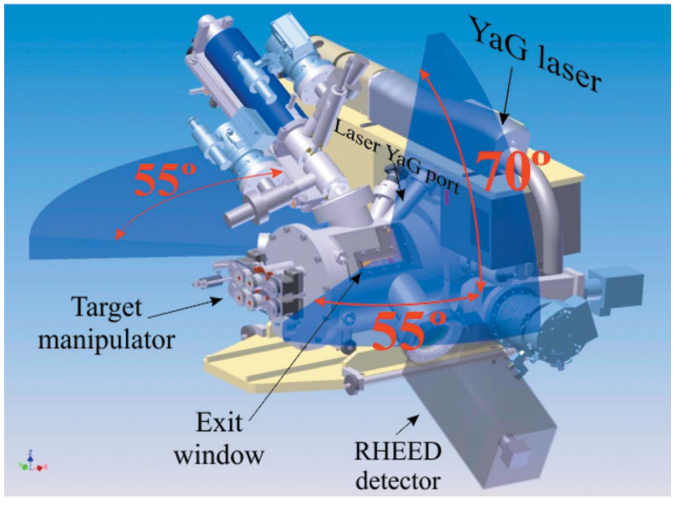

(*b*)

Figure 1
Three-dimensional model of the PLD growth chamber from (*a*) the entrance and (*b*) the exit windows. Different components, such as the Nd:YAG laser, RHEED gun, sample manipulator and RHEED detector, are labeled. The available angular range in the horizontal plane of 55° for coplanar geometry and in the vertical plane of 70° for the non-coplanar geometry is shown in (*b*).

Regarding the components of the PLD chamber shown in Figs. 1(*a*) and 1(*b*), a high-power compact Q-Switched Nd:YAG laser supplied by Quantel-Laser (Les Ulis, France) is mounted on the support frame of the system. A sliding mount allows for easy addition or removal of the non-linear optical elements for operation at 1064, 532 and 266 nm laser wavelengths. The laser beam is focused onto the target with a motorized focus lens *via* a motorized mirror. The lens position and mirror angle change automatically with the substrate–target distance to maintain a constant fluence and beam position on the target. The target manipulator holds eight different targets ready for operation, enabling a sequential heteroepitaxy of diverse multilayer and superlattice structures.

Similarly to other *ex situ* PLD chambers, our *in situ* chamber is equipped with a differentially pumped RHEED gun operational up to 30 kV and a RHEED screen for imaging the electrons from the RHEED gun diffracted on the sample surface. The RHEED vacuum assembly is separated from the main chamber by two small apertures, with each stage pumped by a turbomolecular pump. The RHEED gun is mounted on a moveable platform which allows for the adjustment of electron beam position and angle of incidence by means of two stepper motors. The RHEED set-up is a useful feature, as it permits optimizing the growth parameter prior to the *in situ* synchrotron studies, which can be a time-consuming process (see, for example, Bi *et al.*, 2008).

The distance between the target and the substrate can be adjusted to between 35 mm and 100 mm. The manipulator supports the target rotation and a sideways toggling motion for even target wear. The manipulator flange can be opened and the whole assembly can be slid out on two rails for easy access and target exchange.

The load lock chamber holds a sample storage rack that can hold up to six samples. The whole load lock assembly can be detached from the main chamber in case the main chamber is opened.

As illustrated in Figs. 2(*a*) and 2(*b*), the chamber was designed to be coupled to the heavy duty diffractometer, which features two different detection systems such as a Mythen 1K single-photon-counting linear detector as well as a Pilatus 100K two-dimensional pixel detector from Dectris in Switzerland. The possibility to swap between these two detection systems will ensure an efficient use of the beam time in future investigations as it is fast enough to successively record 2D-RSMs and 3D-RSMs during the growth process.

In Fig. 2(*a*) the Mythen 1K linear detector shown is used to detect the diffracted beam in the horizontal plane. This represents the coplanar diffraction geometry appropriate for measuring symmetric and asymmetric reflections. The Pilatus 100K detector is positioned in the vertical plane where the scattered beam could be detected with a diffraction angle up to 70°. This corresponds to the non-coplanar geometry, where it is possible to measure the diffraction from crystalline planes perpendicular to the sample surface. This geometry is called grazing-incidence diffraction. It should be pointed out that both geometries could only be measured separately due to the

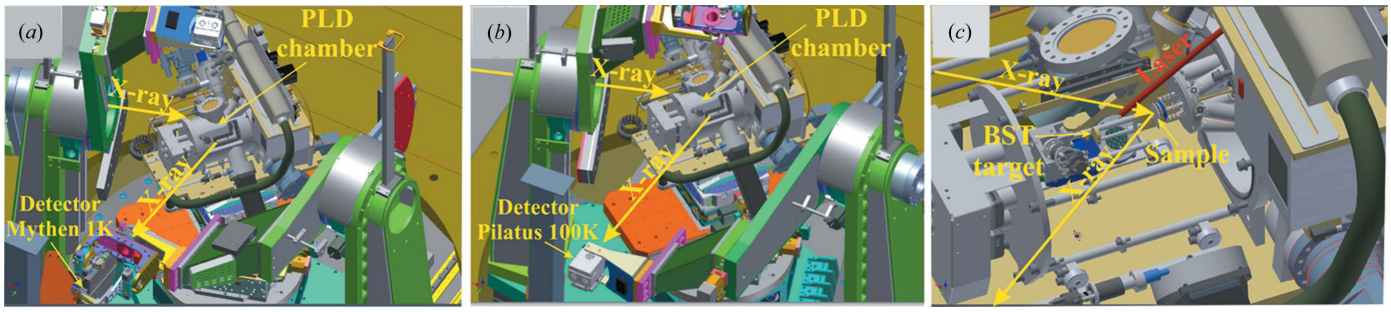

Figure 2
Three-dimensional models of the *in situ* synchrotron PLD chamber combined with the multipurpose heavy duty diffractometer installed at the NANO beamline, located at the synchrotron facility ANKA, Germany, where the linear detector and the two-dimensional detector Pilatus 100K could be used successively during the PLD growth. (*a*) The coplanar X-ray diffraction geometry used in the *in situ* PLD growth of (BST, $x = 0.5$) on MgO. (*b*) The two-dimensional detector positioned in the vertical plane with an angular range up to 70° corresponding to the non-coplanar diffraction geometry. (*c*) Three-dimensional model of the open *in situ* PLD chamber showing the hexapod as a sample manipulator used to align the sample with respect to the incident beam and to rotate the sample 360° around the surface normal. The sample surface is positioned vertically.

difference in the incidence angle of the sample in the diffraction condition. In the current investigation, only the Mythen 1K detector has been used to perform the 2D-RSMs (see Fig. 2*a*).

Fig. 2(*c*) shows the deposition chamber, opened and pulled out on the two rails. The sample is mounted vertically on a substrate manipulator which consists of a hexapod and a rotation stage, enabling the alignment of the substrate with respect to the incoming beam with a precision of 0.001°. The diffraction plane corresponds to the plane containing the surface normal, the incident scattering wavevector and the scattered wavevector. Since the sample surface orientation is vertical, the diffraction plane would be the horizontal plane corresponding to a scattering angle of 55°, measured between the sample surface and the diffracted wavevector.

2.3. *In situ* high-resolution X-ray diffraction at the NANO beamline

The synchrotron X-ray diffraction measurements were carried out at the NANO beamline at the synchrotron facility ANKA (Karlsruhe, Germany) dedicated to high-resolution X-ray diffraction, surface and interface scattering. The beam was focused at the sample to 200 µm horizontally and 80 µm vertically using the two last cylindrical mirrors of the beamline optics. The estimated horizontal and vertical divergences are 0.315 mrad × 0.2 mrad full width at half-maximum (FWHM). X-ray diffraction experiments were carried out at an energy of 10 keV with an energy resolution of 10^{-4} using a Si (111) monochromator. In order to explain the diffraction geometry used in the *in situ* X-ray characterization during PLD growth, the sample and detector motions shall be introduced first. In fact, the inclination of the sample surface with respect to the incoming beam is performed by rotating the whole chamber along the vertical axis using the rotation circle of the diffractometer [see Figs. 2(*a*) and 2(*b*)]. The incidence angle is limited to 55°, as defined by the opening angle of the entrance window (see Fig. 1*b*).

2D-RSMs of symmetric and asymmetric reflections were recorded by means of rocking curve scans which were carried out by rotating the chamber around the vertical axis under Bragg conditions, while the detector was kept at the respective Bragg diffraction angle. All X-ray data were recorded using a Mythen 1K microstrip solid-state detector, featuring 1280 channels with a channel size of 50 µm and a point-spread function of one channel. The 1280 channels are spread within the horizontal diffraction plane, as given by the horizontal cone defined by the exit windows (see Fig. 2*a*). The 2θ Bragg angle, defined as the angle between the direct and the diffracted beams, can reach up to 110° in this set-up. The angular resolution of the diffracted beam of 0.002° was predefined by the channel size of 50 µm, and the distance between sample and detector was equal to 1456 mm. The 2D-RSMs of the symmetric 002 reflection and the XRR curves were recorded sequentially. For each measurement the growth was interrupted for 10 min to collect XRR and 2D-RSMs data.

The first XRR curve was recorded after 1 min of growth. The acquisition of XRR curves requires about 5 min. In a second step, acquisition of the 2D-RSM of symmetric reflection 002 was performed by rocking the sample around the Bragg angle within 5 min of acquisition time. After 105 min of growth, acquisition of the RSM of asymmetric reflection 113 was performed within about 2 h since the acquisition time per point was increased from 1 s to 10 s in order to obtain better statistics. Additionally, time-resolved diffraction profiles within the time resolution of 1 s were recorded during the growth time by keeping the detector at a fixed position, going through the maximum intensity of the (BST, $x = 0.5$) Bragg peak.

2.4. Atomic force microscopy of $Ba_{0.5}Sr_{0.5}TiO_3$ grown on MgO

Atomic force microscopy (AFM) was performed on the PLD-grown sample after a full deposition time of 105 min, using a UHV AFM (Omicron Nanotechnology) equipped with a contact mode tip. The sample was outgassed for one day under 5×10^{-11} mbar pressure before analyzing the surface. A typical value for the scan speed was 0.5 µm s^{-1}, while the force interaction and loop gain were chosen as 15 nN and 12%, respectively.

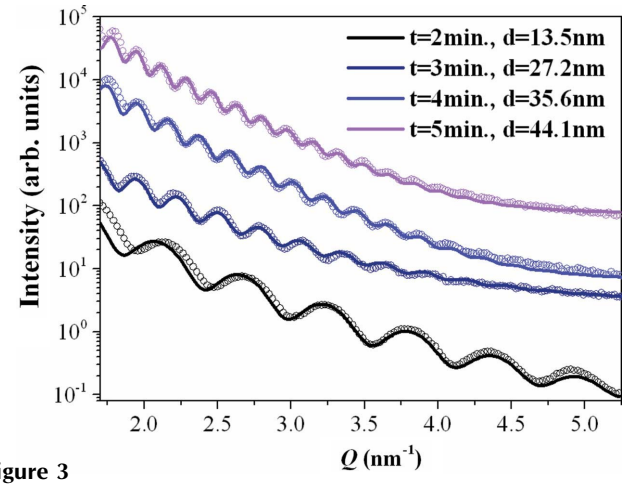

Figure 3
Experimental XRR curves indicated by open circles and the fitting profiles obtained using the Bruker *Leptos* software package. The XRR curves were recorded after growth times of 2, 3, 4 and 5 min. The derived thicknesses from the fitting process indicate an average growth rate of 8.4 nm min^{-1}.

3. Results and discussion

3.1. *In situ* XRR measurement

XRR curves were recorded after 2, 3, 4 and 5 min of growth. The growth was interrupted during the XRR measurement, which lasted about 5 min, to follow the evolution of the film thickness as well as the change in surface and interface roughness during the PLD growth up to 5 min.

The data presented in Fig. 3 were derived from 2D-RSMs where $Q_x = Q_y = 0$, corresponding to the specular scattering recorded for the first 5 min of the PLD growth. It should be emphasized that only the growth time is indicated in Fig. 3; during the acquisition time of XRR measurements no further growth took place.

The XRR curves have been shifted vertically in Fig. 3 for better clarity. The film thickness, and thus the growth rate (nm min^{-1}), were determined from the periodicity of the Kiessig fringes. In order to accurately determine the film thickness and the roughness changes during the PLD growth, a fitting procedure was applied to all reflectivity curves using the Bruker *Leptos* software package.

The growth rates derived from Fig. 3 are 6.8 nm min^{-1}, 9.1 nm min^{-1}, 8.9 nm min^{-1} and 8.8 nm min^{-1}, determined after film growth of 2 min, 3 min, 4 min and 5 min, respectively. An average growth rate of 8.4 nm min^{-1} was found for the growth conditions mentioned above in §2.1.

As the growth time increases, the oscillation period of reflectivity decreases indicating clearly the increase of the film thickness up to about 44.1 nm after 5 min of growth. The surface roughness derived from the fitting varies from 0.36 nm to 0.56 nm while the interface roughness increases from 0.4 nm to 0.8 nm.

3.2. *In situ* X-ray study of the two crystalline phases formation

Fig. 4(*a*) displays the 2D-RSMs of the symmetric 002 reflection recorded during the PLD growth of (BST, $x = 0.5$) on MgO, having a tensile strain of −5.52% at room temperature. The 2D-RSM at $t = 0$ min was recorded once the substrate temperature reached the growth temperature of 1023 K. Thus it solely consists of the signal of the MgO substrate. After applying 600 single laser shots, *i.e.* after 1 min of growth, the RSM was recorded by rocking the sample around its Bragg angle. A detectable single peak originating from the (BST, $x = 0.5$) layer starts to appear at Q_{002} = 3.137 $Å^{-1}$. A further increase in the number of laser pulses applied on the target induces an enhancement of the peak maximum intensity and an increase in the lateral broadening of the reflection. Moreover, a splitting of the peak into two peaks takes place in the transverse direction, indicating the presence of a new phase with different unit-cell parameters [see RSM of Fig. 4(*a*) at 105 min].

From the RSMs shown in Fig. 4(*a*), the profiles along the crystal truncation rods (CTRs) (at $Q_{110} = 0$) were derived and plotted in Fig. 4(*b*) (vertical shifted for clarity). Since the lattice parameter of the substrate MgO is 4.212 Å (at room temperature) and the average thermal linear expansion coefficient is 8×10^{-6} K^{-1}, the lattice parameter of the cubic unit cell of MgO at growth temperature of 1023 K is 4.243 Å. The corresponding reciprocal space coordinates of the symmetrical reflections 002 are given by

$$Q_{002} = 2\left(2\pi/c_{\mathrm{MgO}}\right) = 2.96\ Å^{-1}, \quad (1)$$

where c_{MgO} is the unit-cell lattice constant.

All RSMs recorded during the PLD growth up to 105 min confirm that the location of the 002 peak intensity for the MgO substrate remains at 2.960 Å (see Fig. 4*a*).

On the other hand, the estimated lattice parameter for the cubic cell of (BST, $x = 0.5$) bulk at 1023 K is determined to be 3.978 Å using the formula $0.5a_{\mathrm{BaTiO3}} + 0.5a_{\mathrm{SrTiO3}}$, where a_{BaTiO3} and a_{SrTiO3} are the in-plane parameters calculated for the deposition temperature, using the corresponding thermal linear expansion coefficients of 6.2×10^{-6} K^{-1} and 9×10^{-6} K^{-1}, respectively.

In this case, the corresponding reciprocal space coordinates of the reflection 002 are given by

$$Q_{002} = 2\left(2\pi/c_{\mathrm{BST}}\right) = 3.15\ Å^{-1}. \quad (2)$$

Consequently, the lattice mismatch at deposition temperature T = 1023 K can be estimated as follows,

$$f\ (\text{at } 1023\ \mathrm{K}) = \left(\frac{a_{\mathrm{BST}} - a_{\mathrm{MgO}}}{a_{\mathrm{MgO}}}\right) \times 100 = -6.05\%. \quad (3)$$

As Fig. 4(*b*) shows, the CTRs of (BST, $x = 0.5$) do not reveal a peak appearing at Q_{002} = 3.15 $Å^{-1}$ corresponding to c_{BST} = 3.978 Å of the bulk (BST, $x = 0.5$) at 1023 K. In our grown film, the peak corresponding to (BST, $x = 0.5$) becomes detectable (at $t = 2$ min) at Q_{002} = 3.137 $Å^{-1}$ and it moves to lower Q during the growth process. The value of Q_{002} of the peak varies between Q_{002} = 3.137 $Å^{-1}$ (at $t = 2$ min) and Q_{002} = 3.103 $Å^{-1}$ (at t = 105 min) and the corresponding unit-cell parameters are c_{BST} = 4.004 Å at $t = 2$ min and c_{BST} = 4.050 Å at $t = 105$ min. This indicates that the unit cell of (BST, $x = 0.5$)

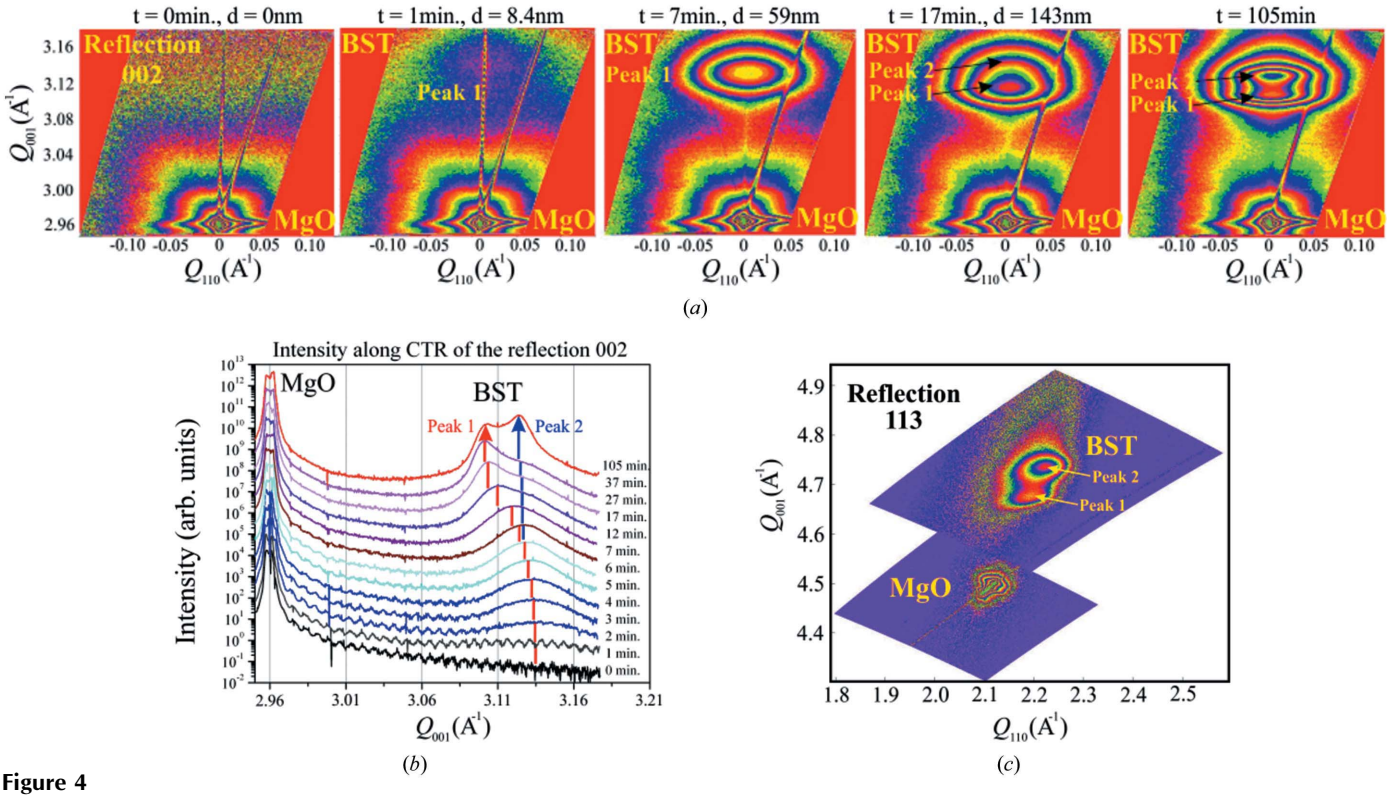

Figure 4
(*a*) Selected 2D-RSMs recorded during the PLD for deposition times of 0, 1, 7, 17 and 105 min. The corresponding film thicknesses for the deposition times 7, 17 and 105 min were derived by considering an average growth rate of 8.4 nm min^{-1} as derived from the XRR measurements. (*b*) Diffraction intensity profiles derived from the 2D-RSMs along the crystal truncation rod (CTR) showing the substrate peak of MgO and (BST, $x = 0.5$) peak 1 shifting continuously by increasing the film thickness recorded during the *in situ* synchrotron PLD investigation of the 002 reflection. The CTR profiles are shifted vertically for better clarity. (*c*) 2D-RSM of the asymmetric 113 reflection after the completion of the PLD growth at $t = 105$ min, showing two distinguishable peaks 1 and 2.

of the high-temperature thin film is larger than that of the unit-cell parameter estimated for the bulk material at 1023 K, and the increase of c_{BST} during the growth reflects a distortion of the crystalline structure, being detected using *in situ* X-ray diffraction measurement of the 002 reflection. Such lattice distortion is due to the lattice mismatch and thermal expansion mismatch between the film and the substrate and oxygen vacancies, which are strongly dependent on the chosen O_2 pressure, as has been demonstrated by Alldredge *et al.* (2007), Kim *et al.* (1999) and Zhu *et al.* (2006).

The profile of the peak starts to be asymmetric at $t = 12$ min. Since the determined average growth rate from XRR is 8.4 nm min^{-1}, the corresponding estimated thickness is found to be about 100.8 nm. By increasing the film thickness the intensity of the second peak located at $Q_{002} = 3.124$ Å^{-1} (*i.e.* 4.020 Å) starts increasing, as demonstrated by the RSM recorded at 105 min in Fig. 4(*a*). From the CTRs of Fig. 4(*b*), the second peak could be reliably detected at $t \simeq 17$ min, when the thickness of the grown film exceeds $h_{critical} \simeq 142.8$ nm, indicating the appearance of a new BST phase with a different out-of-plane unit cell. The in-plane lattice parameter of the grown (BST, $x = 0.5$) thin film was derived by recording the RSM of the asymmetric 113 reflection at the end of the growth process and presented in Fig. 4(*c*). This proves the presence of two distinguishable peaks, peak 1 and peak 2, in addition to the MgO peak, originating from the formation of domains having different crystalline phases. In fact the reciprocal space coordinates of peak 1 corresponding to phase 1 derived from the RSM of the 113 reflection are $Q_{001} = 2.193$ Å^{-1} and $Q_{110} = 4.676$ Å^{-1}. The derived in-plane and out-of-plane lattice parameters are $a_{BST} = 4.052$ Å and $c_{BST} = 4.030$ Å, respectively. In the same manner, the reciprocal space coordinates were determined for phase 2: $Q_{001} = 2.221$ Å^{-1} and $Q_{110} = 4.736$ Å^{-1}, the corresponding in-plane and out-of-plane lattice parameters are $a_{BST} = 3.998$ Å and $c_{BST} = 3.980$ Å, respectively. For both crystalline phases, the in-plane lattice parameter is slightly higher than the out-of-plane one, indicating a tetragonal distortion in the crystalline structure of the (BST, $x = 0.5$).

Alldredge *et al.* (2007) have studied in detail the variation in the degree of structural distortion as a function of the O_2 partial pressure during deposition. It was demonstrated that the structure switched from $c > a$ at low oxygen pressure ($\sim$10 mTorr) to $c < a$ at higher O_2 pressures (>50 mTorr). The use of an oxygen pressure of 51 mTorr (0.067 mbar) in our case has led to structural distortion where $c < a$, similar to the result found by Alldredge *et al.* (2007).

In summary, *in situ* RSMs and *in situ* CTRs demonstrate the shift of peak 1 in the first stage of the growth, followed by the gradual appearance of peak 2 which becomes visible for a film thickness larger than a critical thickness $h_{critical} \simeq 142.8$ nm [see Figs. 4(*a*) and 4(*b*)]. This phenomenon confirms the

domain formation revealed by Jiang *et al.* (2002) using HRTEM performed *ex situ* on completely grown films. The domain formation has been interpreted as an effect induced by the surface-terrace structure of the substrate. The broadening of peak 1 and peak 2 in the angular direction is correlated with the crystallite size distribution. This has also been observed by Jiang *et al.* (2002) by HRTEM and SAED in the form of domains grown on the terraces of the substrate. AFM analysis and reflectivity measurements performed by Kim *et al.* (1999) on two PLD (BST, $x = 0.5$) samples grown on (001) MgO for 5 min and 30 min have shown a domain formation. In fact, the surface roughness of the sample grown for 30 min found by AFM was much larger than that of the 5 min sample. The formation of domains with crystalline structures characterized by different out-of-plane unit-cell parameters results from the poor matching between the (BST, $x = 0.5$) and MgO lattices. The formation of the two distinguished diffraction peaks, belonging to two different crystalline phases in the *in situ* RSMs beyond a critical film thickness, is most probably correlated with the domain formation being considered as an energy minimization process.

Moreover, prior to the splitting of peak 1 into peaks 1 and 2, the position of this peak shifts, indicating the presence of a strain gradient which is forming with an increase in the film thickness. A similar effect has been recorded by Catalan *et al.* (2005) by using X-ray analysis in their *ex situ* study of ferroelectric thin layers of (BST, $x = 0.5$) with different thicknesses. It should be emphasized that the critical thickness leading to the formation of two crystalline phases with different lattice parameters is different from the determined critical thickness of the few monolayers for the misfit dislocation formation in the case of the system $Ba_{0.5}Sr_{0.5}TiO_3$ on MgO substrates with a lattice mismatch of about −6.05% at a growth temperature of 1023 K.

3.3. Time-resolved measurement of the diffraction profiles of the 002 reflection

To follow up the evolution of the diffraction profile of the 002 reflection with a time resolution of 1 s, we record the diffraction profile along a specific direction in the RSM going through the maximum intensity of peaks 1 and 2 of (BST, $x = 0.5$) and partially through the MgO peak, as illustrated in Fig. 5, using a continuous line D indicating the detector position. The sample and the detector positions were fixed, and using the advantage of a linear detector with 1280 channels it was possible to simultaneously record part of the MgO substrate peak and the two complete peaks of (BST, $x = 0.5$) as indicated in the inset of Fig. 5. A three-dimensional presentation of time-resolved diffraction profiles for the symmetric 002 reflection is given in Fig. 5. Time-dependent scans were recorded during the deposition of (BST, $x = 0.5$) on MgO, showing the appearance of peak 2 beyond a critical thickness and indicating an instability in the morphology of (BST, $x = 0.5$) grown on the MgO substrate.

The time $t_0 = 17$ min corresponds to the critical film thickness of 142.8 nm where a new crystalline phase of (BST, $x = 0.5$) appears. For a deposition time beyond $t_1 = 27$ min, the intensity of peak 2 increases to such a point that it is clearly differentiated from peak 1. For a deposition time longer than $t_2 = 65$ min the intensity of peak 2 increases above peak 1, reflecting the dominance of the new crystalline phase of domain 2. Additionally, the unit-cell parameters could be accurately derived from the peaks' positions.

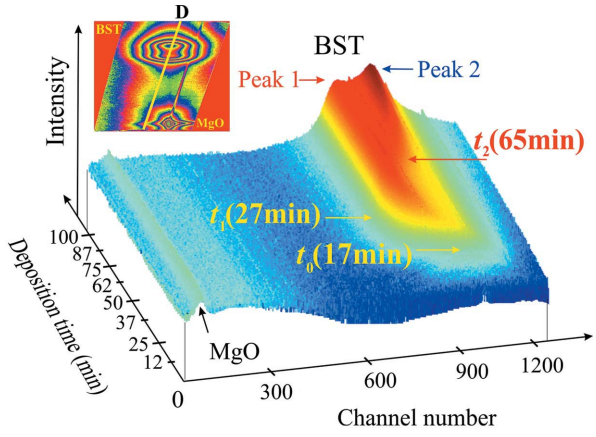

Figure 5
Three-dimensional presentation of the variation of the diffraction intensity measured during the ablation of the (BST, $x = 0.5$) target by the Nd:YAG laser. The intensity profile is recorded by the linear detector Mythen 1K having 1280 channels. The sample is oriented at the Bragg angle for peak 2 and positioned in such a way that we cross the 2D-RSM along the yellow line going through the maximum intensity of peak 2 and partially through peak 1 as shown in the inset. Three main changes were detected at t_0 (17 min), t_1 (27 min) and t_2 (65 min).

3.4. *In situ* determination of domain size and surface morphology

The growth of (BST, $x = 0.5$) on the MgO substrate with a tensile strain of −6.05% at 1023 K was accompanied by the formation of a broad diffracted intensity distribution around the main reflection, due most probably to the presence of defects. The generation of dislocations has been widely accepted as a major mechanism to release this induced strain. Typically, edge dislocations can be formed near the interface due to a full or partial release of the interface strain energy resulting from the lattice misfit between the film and the substrate.

The high-resolution electron microscopy study of Chen *et al.* (2002) revealed that the edge dislocations are uniformly formed along the entire interfaces of ferroelectric (BST, $x = 0.5$) grown on $LaAlO_3$ (001). This type of dislocation is known as a misfit dislocation since it is localized at the film–substrate interface.

The diffraction profiles along the angular direction Q_{110} transverse to the CTR were determined from the RSMs and are presented as a function of the deposition time in Fig. 6(*a*). In their theoretical calculation of the X-ray diffraction profile, Kaganer *et al.* (2009) reported on how the influence of misfit dislocations at the layer–substrate interface contributes to broadening of the symmetric reflections.

In addition to the strain broadening, most materials also generate a broadening due to the finite thickness of the crystals in the direction d_{hkl} of domains over which diffraction is coherent. The broadening given by the FWHM of the diffraction profiles was determined during the PLD deposition procedure and is shown in Fig. 6(*b*). By using the Debye–Scherrer formula (Warren, 1969), the mean size of crystalline domains $L1$ and $L2$ derived from peaks 1 and 2, respectively, have been determined during the *in situ* PLD diffraction measurement. It should be noted that the contribution of misfit dislocations to the broadening was not taken into account and therefore the total broadening of the diffraction profile in the angular direction was attributed only to the formation of the crystalline domains.

The variation of the mean domain sizes $L1$ and $L2$ *versus* the deposition time is illustrated in Fig. 6(*c*). In the first stage of growth, only domain 1 forms, with a mean size $L1$ which increases to about 13.5 nm at t = 17 min when the film thickness reaches 107 nm. Beyond this critical film thickness $h_{\rm critical}$ = 142.8 nm, an instability in the morphology occurs, leading to the generation of a second crystalline domain $L2$ with a mean size of 13.5 nm, which finally reaches a size of 19.4 nm. In comparison, the final size of domain 1 is about 16 nm. This observation confirms the existence of two crystalline domains with different mean lateral sizes. AFM performed on the PLD sample grown for t = 105 min, after cooling to room temperature, reveals a size distribution of the crystalline domains varying between 5 nm and 40 nm (see Fig. 6*d*). The mean domain sizes, measured by AFM, are found to be larger than those derived from the diffraction profile of the 002 reflection at 1023 K. It should be noted that AFM has been performed at room temperature after cooling the sample. However, the influence of the cooling of the (BST, x = 0.5) after the growth has not been studied and the sample morphology seems to change during the cooling process. Additionally, the measured size from the AFM micrograph is convoluted with the cantilever tip with a size of 10 nm.

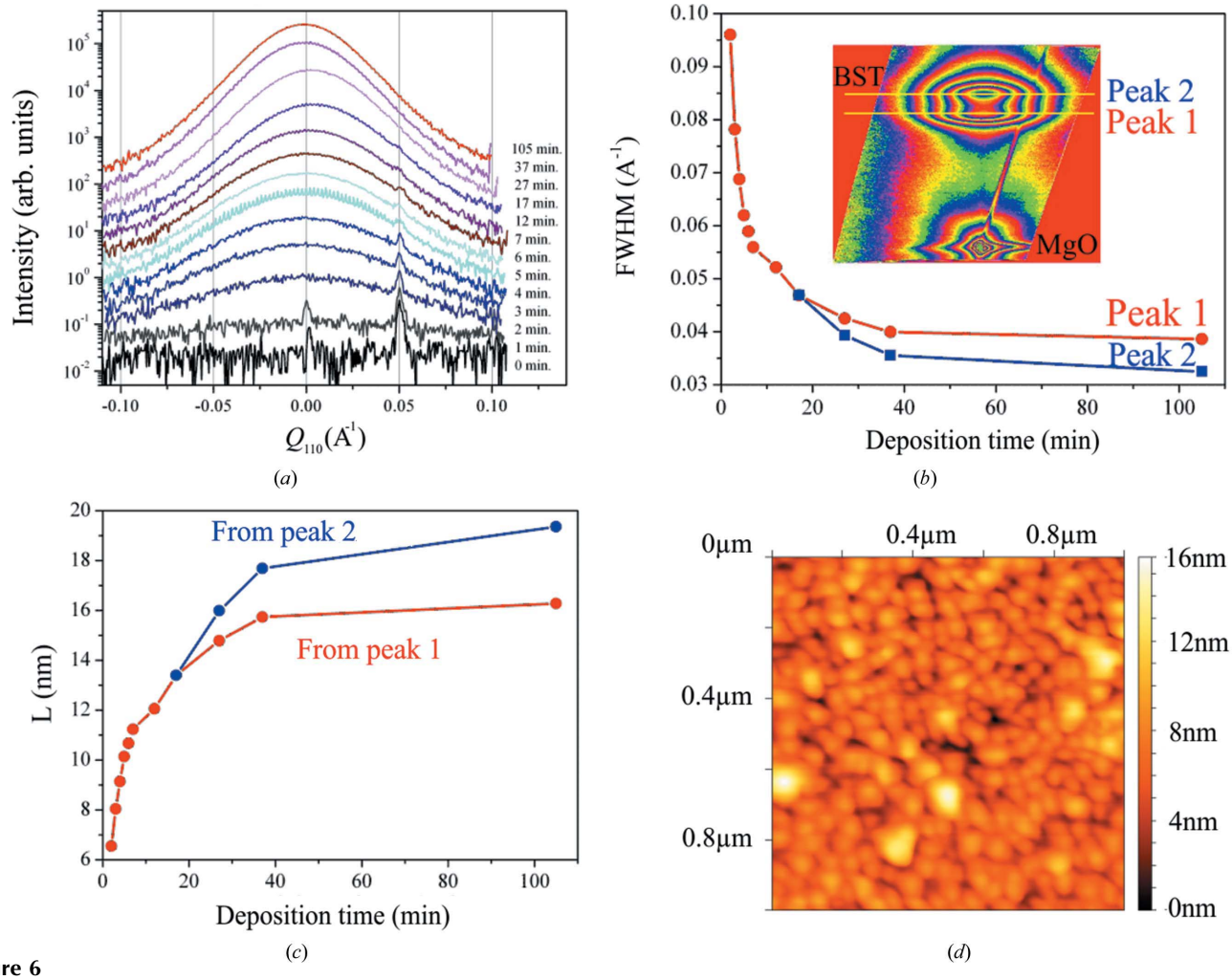

Figure 6
(*a*) Intensity profiles derived from the *in situ* RSMs along the angular direction recorded during the PLD growth of (BST, x = 0.5) on MgO. (*b*) Variation of the broadening of the angular intensity profiles expressed in FWHM with the deposition time. The inset indicates the direction of the cross section along the angular direction for deriving the intensity profiles. (*c*) Increase of the domain sizes with the deposition time derived for peaks 1 and 2. (*d*) AFM of the grown (BST, x = 0.5) on MgO sample for 105 min and after cooling the sample to room temperature, showing the presence of domain formation with a size distribution varying between 5 nm and 40 nm.

4. Conclusions

Time-resolved synchrotron X-ray diffraction allowed us to follow the occurrence of a structural distortion during the PLD growth process with a time scale of 1 s. A shift of the diffraction peak 1 was detected in the growth phase up to a film thickness of 107 nm, demonstrating the presence of an internal strain gradient across the film. Simultaneously, the diffuse scattering around the maximum peak intensity in the 2D-RSMs indicates the strain relieving through the formation of misfit dislocations near the interface between the (BST, $x = 0.5$) and MgO. *In situ* XRR recorded during PLD growth up to 44 nm shows the formation of a sharp interface and smooth surface of the epitaxial grown film of (BST, $x = 0.5$) on the MgO substrate.

By exceeding a critical thickness of 142.8 nm, besides the misfit dislocations at the interface, *in situ* PLD investigation has uncovered the formation of a second crystalline phase. For both identified crystalline phases, the in-plane lattice parameter is slightly higher than that of the out-of-plane, indicating a distortion in the crystalline structure of the (BST, $x = 0.5$) from the cubic to the tetragonal structure as revealed by the 2D-RSM of the asymmetric reflection. The domain formation, being a mechanism for energy minimization in the case of a poor lattice match such as for the (BST, $x = 0.5$) on the MgO substrate with lattice mismatch of -6.05%, has been observed by HRTEM in previous studies.

The *in situ* PLD synchrotron characterization set-up enabled us to understand the influence of the film thickness on the microstructure of the (BST, $x = 0.5$) grown on MgO substrate. The latter has been found to have a strong impact on the dielectric properties.

We would like to acknowledge Mr Tasilo Heeg and Mr Wolfgang Stein from the company Surface (in Hückelhoven, Germany) for their fruitful collaboration and their outstanding proposals to satisfy our specification for the *in situ* synchrotron PLD chamber.

References

Alldredge, L. M. B., Chang, W., Qadri, S. B., Kirchoefer, S. W. & Pond, J. M. (2007). *Appl. Phys. Lett.* **90**, 212901.
Bi, L., Taussig, A. R., Kim, H. S., Wang, L., Dionne, G. F., Bono, D., Persson, K., Ceder, G. & Ross, C. A. (2008). *Phys. Rev. B*, **78**, 104106.
Catalan, G., Noheda, B., McAneney, J., Sinnamon, L. J. & Gregg, J. M. (2005). *Phys. Rev. B*, **72**, 020102.
Chen, H., Lia, L. & Urban, K. (2002). *Appl. Phys. Lett.* **81**, 1291.
Chen, H., Yang, C., Fu, C., Zhao, L. & Gao, Z. (2006). *Appl. Surf. Sci.* **252**, 4171–4177.
Chen, L., Shen, J., Chen, Y., Luo, G. P., Chu, C. W., Miranda, F. A., Van Keuls, F. W., Jiang, J. C., Meletis, E. I. & Chang, H. Y. (2001). *Appl. Phys. Lett.* **78**, 29.
Dale, D., Fleet, A., Suzuki, Y. & Brock, J. D. (2006). *Phys. Rev. B*, **74**, 085419.
Eres, G., Tischler, J. Z., Yoon, M., Larson, B. C., Rouleau, C. M., Lowndes, D. H. & Zschack, P. (2002). *Appl. Phys. Lett.* **80**, 3379.
Findikoglu, A., Jia, Q. X. & Reagor, D. W. (1997). *IEEE Trans. Appl. Supercond.* **7**, 2925–2928.
Fleet, A., Dale, D., Woll, A. R., Suzuki, Y. & Brock, J. D. (2006). *Phys. Rev. Lett.* **96**, 055508.
Jang, S. I., Choi, B. C. & Jang, H. M. (1997). *J. Mater. Res.* **12**, 1327–1334.
Jia, Q. X., Groves, J. R., Arendt, P., Fan, Y., Findikoglu, A. T., Foltyn, S. R., Jiang, H. & Miranda, F. A. (1999). *Appl. Phys. Lett.* **74**, 1564.
Jiang, J. C., Lin, Y., Chen, C. L., Chu, C. W. & Meletis, E. I. (2002). *J. Appl. Phys.* **91**, 3188.
Kaganer, V. M., Brandt, O., Riechert, H. & Sabelfeld, K. K. (2009). *Phys. Rev. B*, **80**, 033306.
Kim, S., Kang, T. S. & Je, J. H. (1999). *J. Mater. Res.* **14**, 2905.
Kim, T. S., Kim, C. H. & Oh, M. H. (1994). *J. Appl. Phys.* **75**, 7998–8003.
Lee, B. T. & Hwang, C. S. (2000). *Appl. Phys. Lett.* **77**, 124.
Lin, Y. & Chen, C. L. (2009). *J. Mater. Sci.* **44**, 5274–5287.
McNeal, M. P., Jang, S. J. & Newnham, R. E. (1998). *J. Appl. Phys.* **83**, 3288.
Okatan, M. B., Cole, M. W. & Alpay, S. P. (2008). *J. Appl. Phys.* **104**, 104107.
Tischler, J. Z., Eres, G., Larson, B. C., Rouleau, C. M., Zschack, P. & Lowndes, D. H. (2006). *Phys. Rev. Lett.* **96**, 226104.
Vonk, V., Konings, S., Barthe, L., Gorges, B. & Graafsma, H. (2005). *J. Synchrotron Rad.* **12**, 833–834.
Wang, H. H., Fleet, A., Brock, J. D., Dale, D. & Suzuki, Y. (2004). *J. Appl. Phys.* **96**, 5324.
Warren, B. E. (1969). *X-ray Diffraction.* Reading: Addison-Wesley.
Willmott, P. R., Herger, R., Schlepütz, C. M., Martoccia, D. & Patterson, B. D. (2006). *Phys. Rev. Lett.* **96**, 176102.
Willmott, P. R., Schlepütz, C. M., Patterson, B. D., Herger, R., Lange, M., Meister, D., Maden, D., Brönnimann, Ch., Eikenberry, E. F., Hülsen, G. & Al-Adwan, A. (2005). *Appl. Surf. Sci.* **247**, 188–196.
Zhu, X. H., Meng, Q. D., Yong, Y. S., He. Y. S., Cheng, B. L. & Zheng, D. N. (2006). *J. Phys. D*, **39**, 2282.